Copper Binding Induces Polymorphism in Amyloid-β Peptide: Results of Computational Models

Dinh Quoc Huy Pham,[†,‡] Mai Suan Li,[*,†] and Giovanni La Penna[*,§,‖]

[†]Institute of Physics, Polish Academy of Sciences, Al. Lotnikow 32/46, 02-668 Warsaw, Poland

[‡]Institute for Computational Science and Technology, 6 Quarter, Linh Trung Ward, Thu Duc District, Ho Chi Minh City 700000, Vietnam

[§]National Research Council Italy (CNR), Institute for Chemistry of Organometallic Compounds (ICCOM), 50019 Florence, Italy

[‖]Italian Institute for Nuclear Physics (INFN), Section of Roma-Tor Vergata, Rome 00133, Italy

ABSTRACT: Amyloid-β (Aβ) peptides are intrinsically disordered peptides, and their aggregation is the hallmark of Alzheimer's disease development. The propensity of the Aβ peptide to intermolecular interactions, the latter favoring different types of oligomers and aggregated forms, has been the object of a huge number of studies. Several facts are now established: the presence of large amount of d-block (M) ions (Zn, Cu, and Fe) in the aggregated forms; the 1:1 M/Aβ ratio favors the formation of amorphous aggregates, with an aggregation rate lower than that in the absence of such ions. In particular, statistical models describing the interactions between copper and amyloid peptides are mandatory to explain the relationship between neuro-degeneration, copper dyshomeostasis, and overproduction of reactive oxygen species, the latter event occurring with aging. In this work, we show, by replica-exchange molecular dynamics simulations, that a copper ion (Cu^{2+}) bound as in the experimentally observed prevailing coordination enhances the probability of closed structures that hinder the formation of extended intermolecular hydrogen bonds that stabilize fibrillar ordered aggregated forms. On the other hand, this effect enhances the catalytic role of the complex during the lifetime of soluble forms.

Cu enhances off-pathway configurations
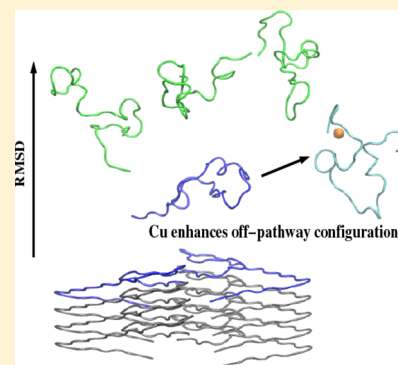
INTRODUCTION

Alzheimer's disease (AD) is the most representative form of dementia in humans.[1] The disease is associated with cognitive degradation caused by neuron death. Molecular events associated with cell death are the aggregation of amyloid-β (Aβ) peptides, of 39−42 aminoacids, to form extracellular fibrils[2] and the accumulation of tau protein intracellularly as tangles.[3]

Aβ peptides are the by-product of amyloid precursor protein (APP) after its cleavage by β- and γ-secretase. The most represented peptides in the pathological AD events are of 40 (Aβ_{40}) and 42 (Aβ_{42}) aminoacids. When observed in vitro in water solution, the short-living monomeric forms of Aβ peptides have no structure, i.e., they are intrinsically disordered proteins (IDPs). Monomers rapidly form relatively soluble oligomers, then highly ordered insoluble protofibrils, and eventually extended fibrils and plaques.[4,5] Soluble oligomers are toxic,[2,6−8] and their role in the pathology is the object of many studies because the potential role in diffusing toxic species before the aggregation process occurs.[9−13] Aβ oligomers are, therefore, early biomarkers of AD.

Metal ions such as zinc, copper, and iron are found at high concentration in fibrils and plaques extracted from the AD-affected area of the brain.[14−18] Metal ions interact with APP and Aβ and, therefore, are potentially important actors before the aggregation of Aβ. Moreover, it has been clearly shown that the 1:1 ratio of Cu/Aβ increases the lag time of insoluble aggregates, thus increasing the lifespan of soluble oligomers.[19] Structural models of such toxic oligomers are of utmost importance to understand the mechanism by which the early events of neurodegeneration trigger the irreversible neuron death, induced for instance by an increased rate in oxidation.[20−23]

The disordered nature of the involved peptides makes any proposal for a structural model for oligomers extremely difficult.[24] Experiments provide important information about the peptide side chains that are involved in interactions with metal ions (electron paramagnetic resonance,[25,26] NMR,[27−29] X-ray absorption spectroscopy,[30] Fourier transform infrared,[31] and small-angle X-ray scattering[32]). As for oligomers, experiments provide average structural characterizations, such as gyration radius (dynamic light scattering[10]) and mobility (mass spectrometry[33] and pI[34]), and the extent of secondary motifs (electron microscopy, atomic force microscopy,[35,36] circular dichroism,[37] and Förster resonance energy transfer[38]). This partial information must be completed with empirical models, but the peptide structural disorder requires extended statistics

Table 1. Temperatures Used in REMD Simulations[a]

280.00, **284.93**, 284.93, 287.41, 289.92, 292.44, 294.97, 297.52, **300.09**, 302.68, 305.28, 307.90, **310.54**, 313.19, 315.86, 318.52, 321.22, 323.95, **326.68**, 329.45, 332.22, 335.02, 337.80, 340.63, **343.48**, 346.35, 349.23, 352.14, 355.06, 358.01, **360.97**, 363.95, 366.95, 369.97, 373.01, 376.07, **379.16**, 382.25, 385.38, 388.52, 391.68, 394.87, **398.07**, 401.29, 404.54, 407.81, 411.10, 414.38, **417.71**, 421.07, 424.45, 427.85, 431.27, 434.72, 438.18, 441.67, 445.18, 448.72, 452.28, 455.87, **459.47**, 463.10, 466.77, 470.45, 474.16, 477.88, **481.64**, 485.42, 489.23, 493.06, 496.91, **500.80**.

[a]The values in boldface are the temperatures used in analysis.

and advanced statistical methods to achieve a proper statistical convergence.[39]

To overtake these limitations, we collected a rich statistics for the $A\beta_{40}$ monomer, both with and without a single Cu^{2+} ion bonded as in the dominant coordination observed with experiments in vitro.[25,26] Before investigating oligomers, a wide statistical description of monomers in the absence and presence of a single Cu ion allows an estimate of the change in configurational landscape induced by the dominant metal ion binding mode. This change has important effects in the properties of the monomer and in the interactions with its environment, inducing, for instance, peptide polymorphism.[40−42]

The $A\beta$ peptide of 40 residues ($A\beta_{40}$), with and without a single bound copper ion in 2+ oxidation state (Cu^{2+}), was simulated with the replica-exchange molecular dynamics (REMD) method.[43] This method greatly enhances the configurational statistics compared to the conventional molecular dynamics for all-atom models of disordered proteins in explicit water.[44] The study will be continued with enhanced sampling techniques.[45,46]

■ METHODS

Replica-Exchange Molecular Dynamics Simulation. The $A\beta$ peptide of 40 residues ($A\beta_{40}$), with and without a single bound copper ion in 2+ oxidation state (Cu^{2+}), was simulated with the REMD method, in order to get the configurational statistics at the physiologically relevant temperature of 311 K. The sequence of $A\beta_{40}$ is:

DAEFRHDSGY$_{10}$ EVHHQKLVFF$_{20}$ AEDVGSNKGA$_{30}$ IIGLMVGGVV$_{40}$ with aminoacids indicated with the one-letter code. To understand the impact of copper binding on the peptide statistics, we used the same starting configurations in both cases. We used the Amber 14 package,[47] with the AMBER99SB[48] force field for the peptide, and TIP3P water model[49] for the explicit water sovent. The AMBER99SB force field is not as good as other force fields (like CHARMM36M) in sampling the configuration space for IDPs.[50] However, the AMBER99SB force field is in better agreement with the experimental data concerning the average β-strand content in amyloid peptides, that is, in the range 12−25%.[37,51] We decided, at this stage, to use the AMBER99SB force field also to compare results with previous simulations analyzed in detail by us.[22] The use of more recent force fields for IDPs will be pursued in the future, after a detailed comparison between experiments and simulations in generalized ensembles will be reported in the context of amyloid proteins. We assumed the physiological (pH ≈ 7) protonation state for aminoacid side chains and free termini. Thus, the charge of $A\beta_{40}$ is −3 (the N-terminus is protonated, and the C-terminus deprotonated). The parameters for copper and copper-bound aminoacids were the same used in our previous MD simulations.[22] Cu is bound to N and O of Asp 1, Nδ of His 6, and Nϵ of His 13; the latter protonated at Nδ. His 14 is neutral and protonated in Nϵ,

similar to His 6. Bond distances and angles involving Cu contribute to harmonic energy terms, with stretching constants, bending constants, and equilibrium value set as fitting parameters of quantum mechanics calculations at the density functional level of approximation for truncated models (see Methods in ref 22). All of the dihedral angles, where Cu has index 2 or 3, do not contribute to the potential energy, whereas those with Cu with index 1 or 4 are obtained by the AMBER99SB force field where heavy atoms have the same dihedral indices of Cu. Point charges are derived from the restrained electrostatic potential method,[52,53] where the electrostatic potential mapped onto the solvent-accessible surface was obtained at the density functional level of truncated models (see ref 22 for details). Excess of net charge obtained by merging point charges of truncated models into AMBER99SB aminoacids was distributed to Cβ and Hβ of Asp 1, His 6, and His 13 when these residues are bound to Cu^{2+}. Lennard-Jones parameters for Cu are reported in the literature.[54]

The REMD simulation was carried out with 72 replicas (or trajectories) corresponding to 72 temperatures ranging from 280 to 500 K. Only 13 temperatures uniformly chosen from the temperature distribution were used for further analysis, and replica at human body temperature, about 310 K, was analyzed in detail.

By using the program TLEAP, within the amber package, initial configurations of $A\beta$ monomer, with and without copper, were inserted in a truncated octahedron cell filled with water molecules, with minimal distance between solute atoms and any edge of 1.4 nm. The initial cell contains 5020 and 4823 water molecules for $A\beta_{40}$ and Cu−$A\beta_{40}$, respectively. The simulation cell was kept neutral by adding the minimal amount of sodium ions, randomly replacing water molecules in the initial configuration. The number of sodium ions was 3 for $A\beta_{40}$ and 2 for Cu−$A\beta_{40}$ because in the latter case, Cu^{2+} replaces one proton in Asp 1 N-terminus. The sizes of the cells were large enough to avoid any direct interaction between the peptide and its periodic image during simulations. The shortest distance between any atom in the solute peptide and its periodic image was never below the direct-space cutoff distance of nonbonding interactions (8 Å). To remove eventual bad contacts produced by the initial solvation, 25 000 steps of steepest decent followed by other 25 000 steps of conjugate gradient minimization were done with a weak restraint applied to the backbone atoms of the solute. The minimized structure was distributed among the 72 replicas, and each replica was equilibrated in 200 000 steps at the temperature chosen in the temperature distribution used in REMD (see below). After equilibration, the REMD simulation was carried out for all replicas for a total time of 200 ns.

For the production, the canonical ensemble was applied and the exchange was attempted every 500 steps of simulation, using a time step of 2 fs. Temperature was controlled by a Langevin thermostat[55] with a collision frequency of 2 ps^{-1}. The SHAKE algorithm[56] was applied to constrain bonds involving

hydrogen atoms. A cutoff of 8 Å was applied for nonbonded interactions, and the particle mesh Ewald algorithm[57] was used to compute long-range Coulomb interactions.

The temperature distribution used in REMD is reported in Table 1, the temperatures used for analysis are emphasized in boldface. The storage of 13 temperatures among the 72 simulated replica was forced by the huge amount of disc space required by the analysis. We applied the weighted-histogram analysis method[58] to energy data. The behavior of average potential energy and heat capacity (data not shown here) as a function of temperature T is strongly affected by the behavior of the water solvent, that is, not correctly modeled at the low temperatures included in the REMD simulation (see Table 1). The REMD simulation performed in this work is not sufficiently statistically robust to estimate the possibility of thermally induced order-disorder transitions in the protein because the force field, including that used to model the water solvent, is reliable at temperatures close to 298 K. The REMD simulation is used here mainly to capture the statistical contribution of extended protein configurations that are rarely sampled in the temperature range where the force field is accurate. The difference in this sampling due to Cu binding is the unique goal of this REMD application.

The acceptance rate of REMD simulations was, on average, 28 and 29% for, respectively, $A\beta_{40}$ and $Cu-A\beta_{40}$. In order to check that our trajectories are approximately at equilibrium, we divided the averaging time in two windows $[t_{eq}, t_{eq} + (t_{total} - t_{eq})/2]$ and $[t_{eq}, t_{total}]$. In our case, as it will be reported below, $t_{eq} = 60$ ns, whereas $t_{total} = 200$ ns. We assume the convergence of averages when results obtained in these two windows are equal within error bars.

■ ANALYSIS

Root-Mean-Square Deviation. The analysis of root-mean-square deviation[59] (RMSD, see Figure 1, left for $A\beta_{40}$,
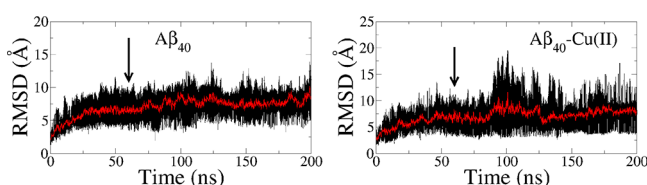

Figure 1. RMSD evolution of $A\beta_{40}$ (left) and $Cu-A\beta_{40}$ (right) at 311 K. The arrow indicates the starting time used for analysis.

right for $Cu-A\beta_{40}$) with respect to the initially equilibrated structure (i.e., before REMD is started) shows a significant time dependence. According to the error analysis summarized above, we calculated the content of secondary motifs for two windows with different values of t_{eq}. This calculation indicates that at $T = 311$ K, the equilibration time t_{eq} is 60 ns (the arrows displayed in the figure) and the averages can be obtained in the range $[60, 200]$ ns.

Secondary Structure. The secondary structure was calculated with the define secondary structure of protein method (DSSP),[60] as implemented in the AmberTools package. The calculation gives eight different kinds of structure: parallel β-sheet, antiparallel β-sheet, α-helix, 3−10 helix, π-helix, turn, bend, and coil. Parallel β-sheet and antiparallel β-sheet are assembled into a β-strand content.

Solvent-Accessible Surface Area. Solvent-accessible surface area (SASA) was calculated with the LCPO method[61] using the CPPTRAJ program in AmberTools.

Gyration Radius and Shape Tensor. The gyration radius (R_g) is defined as the average of square distance between all of the solute atoms and the geometrical center of the same set of atoms. The shape of the solute peptide is analyzed via the three eigenvalues of the rank-2 gyration tensor $\mathbf{S}$[62]

$$S_{\alpha,\beta} = \frac{1}{N} \sum_{i=1}^{N} \mathbf{r}_{i,\alpha} \mathbf{r}_{i,\beta} \tag{1}$$

with i running over the N atoms and α and β running over the three cartesian components of atomic positions $\mathbf{r}$, the latter is with respect to the geometrical center of the selected molecule. The matrix elements of S are averaged over the analyzed configurations in the trajectories, as for the gyration radius. The ranking of $\mathbf{S}$ eigenvalues allows the identification of the shape as oblate (discoidal) or prolate (cylindrical) ellipsoid. The asphericity b and the relative shape anisotropy K^2 are used to quantify the shape anisotropy

$$b = \lambda_3 - \frac{1}{2}(\lambda_1 + \lambda_2) \tag{2}$$

$$K^2 = 1 - 3 \frac{\lambda_1\lambda_2 + \lambda_2\lambda_3 + \lambda_3\lambda_1}{(\lambda_1 + \lambda_2 + \lambda_3)^2} \tag{3}$$

with λ the eigenvalues of $\mathbf{S}$ in descending order. In order to better visualize the distribution of asphericity, we shall define the effective gyration radius, $R_{g,eff} = 2\sqrt{-b}$, that approaches the gyration radius when the solute is isotropic in shape.

End-to-End Distance. End-to-end distance (d_{ee}) is defined as the distance between N(Asp 1) and C(Val 40).

Hydrogen Bonds. Hydrogen bonds are defined when the X−Y distance in X−H⋯Y is smaller than 3 Å and the X−H⋯Y angle is larger than 135°.

Salt Bridges. The number of contacts between positively and negatively charged groups [salt bridge (SB)] is measured with the following equation[63]

$$SB = \sum_{i,j} s_{i,j}$$

$$s_{i,j} = 1 \qquad \text{if } r_{i,j} \leq 0$$

$$= 0 \qquad \text{if } r_{i,j} > 0$$

$$r_{i,j} = |\mathbf{r}_i - \mathbf{r}_j| - d_0 \tag{4}$$

with i and j running over, respectively: Nη (Arg), Nζ (Lys), and the terminal N (when no Cu is present); Cγ (Asp), Cδ (Glu), and the C terminus (Val 40). The d_0 parameter is defined according to the peaks identified in the radial distribution functions for the respective sets of atoms. The value of $d_0 = 0.4$ nm is used in this work.

Ion Mobility Cross Section. Ion mobility cross sections are obtained from the drift times reported in Figure 3A of ref 33 for the species MON^{4+} and Cu−MON^{4+}. We used eq 1 of ref 64 to convert drift time into cross section, with parameters X and c obtained for species MON^{4+} and data reported in Table 1, columns 6−7 and 16−17, ref 64. The charge of ions generated, observed, and assigned in mass spectrometry (+4) is due to the mechanism of ionization in the spectrometer. Thus, the charge is not directly related to the net charge of the
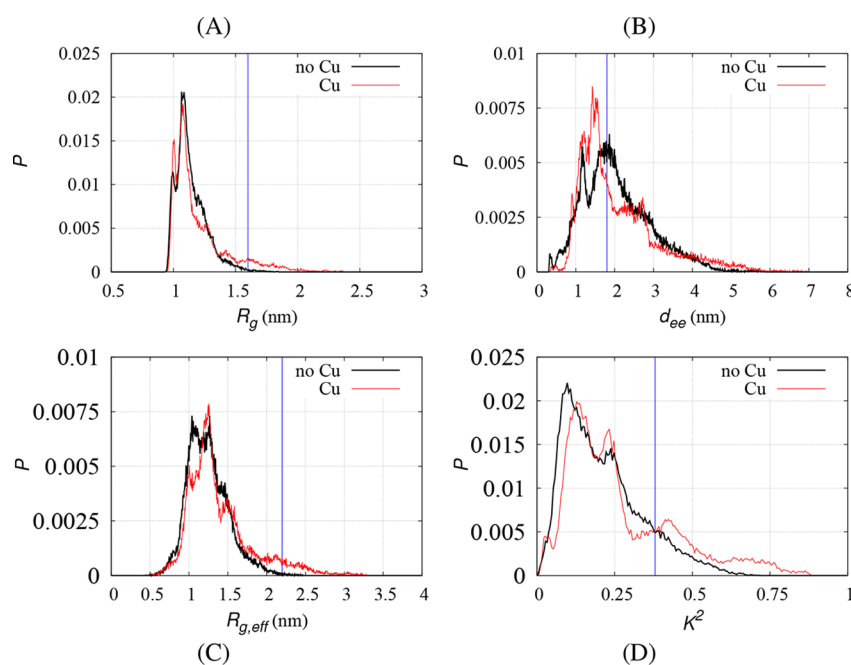
Figure 2. (A) Distribution P of gyration radius of $A\beta_{40}$ (black) and $Cu-A\beta_{40}$ (red) at T = 311 K. Same comparison for the distribution of end-to-end distance (B); effective gyration radius $R_{g,eff}$ (C); and relative shape anisotropy K^2 (D). The vertical bars display the values for the monomers in the most recent fibril structure (PDB 5OQV[65]).

species observed at physiological conditions (−3 and −2 for $A\beta_{40}$ and $Cu-A\beta_{40}$, respectively).

Free-Energy Landscape. Free-energy landscape showed in the main paper is computed as a function of end-to-end distance ($X_1 = d_{ee}$) and RMSD ($X_2 = \text{RMSD}$) with respect to peptide configurations extracted from a proposed fibril structure (see main text for details). The landscape was divided into a 200 × 200 grid in the chosen variables, $\mathbf{X} = \{X_1, X_2\}$. The count of samples within each point in the grid ($N(\mathbf{X})$) is the measure of the free energy A at temperature T for the pair of values in the chosen variables, $\mathbf{X}$

$$A(\mathbf{X}) = -k_B T(\ln N(\mathbf{X}) - \ln N_{max}) \quad (5)$$

where $N(\mathbf{X})$ is the number of configurations with values $\mathbf{X}$ and N_{max} are the number of configurations in the grid point with maximal number of configurations.

■ RESULTS

The average of the gyration radius $\langle R_g \rangle$ at T = 300 K for $A\beta_{40}$ is 1.1 ± 0.1 nm, and at T = 311 K, the physiological working temperature of amyloid peptides in the synaptic region, the average does not change. This value is only slightly larger than the value derived by dynamic light scattering experiments at T = 298 K, reporting a hydrodynamic radius of 0.9 ± 0.1 nm for the monomer.[10] The average gyration radius of 1.2 ± 0.1 nm for $Cu-A\beta_{40}$ at T = 311 K shows that the effect of Cu binding is larger than the increase of 10 K in temperature. In Figure 2, we report the distribution P at T = 311 K of gyration radius R_g (Figure 2A) and of end-to-end distance $d_{ee} = d[\text{N(Asp 1)}-\text{C(Val 40)}]$ (Figure 2B) for the two simulations. As a term of comparison, we display the values of R_g and d_{ee} for the 1−40 region in the monomer as in the most recent $A\beta_{42}$ fibril structure (protein data bank, PDB, 5OQV),[65] as vertical bars in Figure 2A,B. We use the 5OQV structure because it is the unique PDB structure with an organized complete N-terminus. The distribution of gyration radius of $A\beta_{40}$ computed in the

simulation displays a first peak corresponding to 1.0 nm and a second broad peak centered at 1.1 nm. The presence of Cu bound to $A\beta_{40}$ induces only a very small shift in the positions of the first two peaks that remain at 1.0 and 1.1 nm, but the peak at smaller distance (1.0 nm) is significantly more pronounced than that with no Cu. Also, a more significant broadening of the distribution occurs at larger R_g values, beyond 1.5 nm.

Information concerning the size distribution of $A\beta_{40}$ monomers and oligomers, both with and without Cu bound to the peptide, is provided by ion mobility studies.[33] As for monomers, ions with charge 4 have been identified and investigated (Figure 3A in ref 33).

These data reveal two separated conformations for monomeric $A\beta_{40}$, compact and extended, with ion mobility cross sections reported in Table 2. The effect of Cu binding is

Table 2. Ion Mobility Cross Sections (CS) Obtained at T = 311 K Selecting N_c Configurations with the Corresponding Values of Gyration Radius (R_g), Compared to Experimental Values (Last Column)[a]

configurations	N_c	R_g	CS	CS (exp.[33])
$A\beta_{40}$	15	1.0	750 (12)	647
$A\beta_{40}$	18	1.1	781 (21)	689
$Cu-A\beta_{40}$	8	1.0	764 (20)	647
$Cu-A\beta_{40}$	11	1.1	786 (11)	710

[a]Errors within brackets are rms errors over the N_c configurations.

increasing the statistical weight of compact conformations and to slightly shift the cross section of extended conformations. To compare with these results, we measured the ion mobility cross section with the trajectory method implemented in the MobCal code[66−68] (see "Methods" for details). We separated bundles of configurations contributing to the two peaks displayed by $P(R_g)$, at 1.0 and 1.1 nm. The comparison (Table

2) shows that despite the shift between computed and experimental values, the effect of Cu binding is to increase the weight of the cross section arising from compact structures, i.e., those configurations contributing to the lower gyration radius. Also, the spread of the population toward higher values of R_g when Cu is bound to the peptide (Figure 2A) contributes to a higher average extension of the extended conformation, as displayed by experimental data.

As for the end-to-end distance (Figure 2B), the difference between the two distributions is more significant. $A\beta_{40}$ displays a peak at a short distance (0.3 nm) that represents the SB between N- and C-termini, charged in the Cu-free monomer. Broader peaks are displayed at larger distances, with most of the configurations representing the end-to-end distance in the range $1.5 < d_{ee} < 2.0$ nm, that is, around the value displayed by the most recent fibril configuration where the N-terminus has been resolved by electron microscopy (PDB 5OQV[65]). The PDB structure 5OQV ($A\beta_{42}$) reports a configuration for the N-terminus bent toward the C-terminus. This shape is summarized as L–S shape. When in this shape, the $A\beta_{42}$ peptide is flat, with no intramolecular hydrogen bonds, and displays intermolecular head-to-tail electrostatic interactions similar to N(Asp 1 E)–C(Ala 42 B). The PDB structure 2M4J,[69] derived by solid-state NMR of $A\beta_{40}$, also reports the position of the N-terminus, but characterized by significant disorder that does not allow a structural comparison including N-terminus. Because of this, as for the N-terminus, we shall use the PDB structure 5OQV as a reference for comparisons when Cu is not bound to the peptide. In our calculation, the presence of Cu bound to $A\beta_{40}$ induces a marked shift of the broad peak toward 1.5 nm, and the occurrence of the additional marked peak at 0.9 nm in the distribution.

The shape of the peptide can be analyzed using asphericity, b, and relative shape anisotropy, K^2[62] (see "Methods" for details). Asphericity is here reported as the effective radius of gyration, $R_{g,eff} = 2\sqrt{(-b)}$. We remind that values of K^2 close to zero represent isotropic molecules, whereas $K^2 \simeq 1$ represent prolate molecules. Values of $K^2 \simeq 1/4$ represent planar polygonal and oblate molecules. The deviation of $R_{g,eff}$ from R_g (Figure 2A) measures the propensity for the peptide to behave differently from the sphere with average radius R_g. To search for emerging propensity for flat shape within the collected sample at $T = 311$ K, we plot in Figure 2C,D the distribution of $R_{g,eff}$ and K^2, respectively, of the peptide without and with bound Cu. $A\beta_{40}$ is more spherical than Cu–$A\beta_{40}$. When Cu is bound to the peptide, the size of the peak at about 1.25 nm, shifted with respect to the first peak in the distribution of R_g ($\simeq 1$ nm, Figure 2A), increases. Moreover, the tail of the distribution also increases. In $A\beta_{40}$, spherical and aspherical configurations are not separated by hindered configurations, which is the distribution almost represented by a unique broad peak. These features indicate for Cu–$A\beta_{40}$ a propensity to populate at $T = 311$ K different aspherical peptide conformers that are connected through more spherical ones.

The analysis of K^2 shows that asphericity of Cu–$A\beta_{40}$ is associated with prolate shapes. The distribution of relative shape anisotropy, K^2 (Figure 2D), has a larger density at smaller values when Cu is absent than when Cu is bound, meaning a larger propensity for isotropic shapes when no Cu is bound to the peptide. The distribution for Cu–$A\beta_{40}$ shows at least one more peak at $K^2 \simeq 0.4$, with a small peak appearing at

low values of K^2. In summary, the distribution of K^2 reveals the presence of different shapes induced by the Cu binding in $A\beta$. The increase in the population of prolate conformers is due to a decrease in population of isotropic shapes, together with a slight decrease of planar configuration (at $K^2 \simeq 1/4$). On the other hand, the Cu-free peptide shows a more pronounced peak at $K^2 \simeq 0.1$, thus representing a population concentrated around isotropic configurations. The distributions of K^2 for $A\beta_{40}$ and Cu–$A\beta_{40}$ become similar at $T \simeq 380$ K (data not shown here).

In Table 3, we report for both molecules the hydrogen bonds involving N–H amide bonds as donors, displaying a

Table 3. Comparison between Backbone NH Hydrogen Bond Population (%) Obtained at $T = 311$ K for $A\beta_{40}$ When Cu Is Absent (No Cu) and Present (Cu)

N–H bond	acceptor	P (no Cu)	P (Cu)
Ala 2	Oδ (Asp 1)		40
Arg 5	O (Ala 2)		36
His 6	O (Glu 3)	11	27
Gly 9	Oδ (Asp 7)	11	22
His 13	O (Tyr 10)		60
His 14	O (Tyr 10)		39
His 14	Ot (Val 40)	19	
His 14	O (Val 40)	21	
Gln 15	O (Val 18)		48
Lys 16	O (His 13)	33	15
Leu 17	O (His 13)	15	67
Val 18	O (His 13)		28
Phe 20	O (Leu 17)	14	
Gly 25	Oδ (Asp 23)	13	15
Ser 26	Oδ (Asp 23)	11	11
Ser 26	O (Asp 23)	13	12
Asn 27	O (Asp 23)	20	
Gly 29	Oδ (Asn 27)	13	
Ala 30	O (Asn 27)	16	
Ile 31	Oδ (Asn 27)	12	
Leu 34	O (Ile 31)		15
Met 35	O (Ile 31)		12
Gly 37	O (Leu 34)	11	
Val 40	O (Val 12)	14	
sum		247	447

probability P larger than 10% at $T = 311$ K. Three regions are emphasized: the N-terminal region containing the essential Cu-binding segment (1–16); the central hydrophobic segment (17–21) that is known as the essential initiation segment for extended β-sheet formation; and the C-terminal region (22–40) containing the loop-forming segment (Glu 22/Asp 23/Lys 28) and the C terminus, Val 40. It can be noticed that many hydrogen bonds involving the C-terminus (22–40) are demolished by the presence of Cu bound to Asp 1, His 6, and His 13, with a little recovery in the 34–35 region. This change is due to the formation, with Cu, of many hydrogen bonds within the 1–16 segment, constrained in phase space by the involvement of side chains in Cu binding. Interestingly, also Val 18 is significantly affected by His 13 when the latter is bound to Cu. Consistently, His 13 is diverted from Lys 16 by Cu binding. Assuming the hydrogen bonds as independent, the sum of the percentage (last row in the table) clearly shows that the number of intramolecular hydrogen bonds is, with Cu, about twice that without Cu. Summarizing, the Cu binding
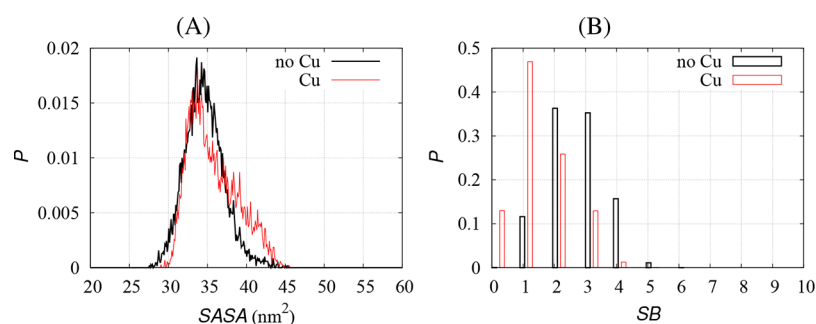
Figure 3. (A) Distribution (P) at $T = 311$ K of SASA: Aβ_{40} (black); Cu−Aβ_{40} (red). (B) Same comparison for the distribution of SB.

enhances the probability to form intramolecular hydrogen bonds involving the peptide backbone, thus hindering the chance to form those intermolecular hydrogen bonds that are observed in fibril structures.

In Figure 3A,B, we plot, respectively, the distribution, at $T =$ 311 K, of SASA and of the number of contacts between positively and negatively charged groups (SB). These plots confirm the previous observations, obtained by canonical MD simulations,[22] concerning the positive effect of Cu binding on the solvent accessibility that increases with Cu binding (Figure 3A), and the inverse effect on the number of intramolecular electrostatic interactions that decreases markedly when Cu is bound to the N-terminus (Figure 3B). The average SASA is 34.6 ± 2.5 and 35.7 ± 3.1 nm^2, respectively, for Aβ_{40} and Cu−Aβ_{40}. The effect of Cu binding is to let charged side chains pointing toward the water solvent and the ionic atmosphere. The analysis of the number of water molecules within the first two peaks of radial distribution function ($d \leq 0.4$ nm, data not shown here) is also consistent with this information.

We searched into the trajectories for configurations resembling those present in experimental structures of aggregated states of Aβ. The common structured segment of the peptide present in all of the experimental structures reported in the PDB is 17−40. It is also recognized that a key feature in Aβ_{40} aggregation is the formation of a significantly long β-strand in region 30−40, assisting the formation of a U-shaped β-sheet involving regions 10−22 and 30−40.[70−72] The comparison concerning these structural features is reported in Table 4. The data clearly show that the introduction of Cu into the peptide hinders the formation of S-like configurations in the C-terminus, thus suppressing the intermolecular inter-actions that stabilize the fibrillar state. The presence of Cu decreases the population of the so-called fibril-prone state,[73] slowing down self-aggregation. This effect is correlated with the increase of NH intramolecular hydrogen bonds (Table 3) and to the release of intramolecular SBs when Cu is bound to the peptide (Figure 3B). The latter event has been recognized as particularly important to explain the earlier onset of AD in the Iowa mutant of Aβ, where the mutation D23N and the breaking of the Asp 23−Lys 28 SB enhance the formation of an antiparallel β-sheet in the C-terminus.[46,74] This antiparallel β-sheet is less fibril prone compared to the parallel β-sheet structure adopted by Aβ in most of the fibril structures.[46]

The free-energy landscape is displayed in Figure 4, as a function of end-to-end distance d_{ee} and RMSD with respect to the reference chain C in model 1 of PDB 5OQV. The comparison between left panel in Figure 4 (with no Cu) and right panel in Figure 4 (with Cu) clearly shows that at $T = 311$ K, the Cu binding introduces structure in the peptide: 6 peaks

Table 4. Percentage of Configurations at $T = 311$ K with: (i) RMSD of Backbone Heavy Atoms <4 Å with Respect to Structures of Monomers Extracted from Experimental Fibril Structures in the PDB (PDB Code in First Column); and (ii) Displaying β-Strand Conformation (Last Row)^a

reference PDB	peptide	shape	no Cu	Cu
2MXU	Aβ_{42}	S	0.14	0.00
2NAO	Aβ_{42}	S	0.29	0.00
5KK3	Aβ_{42}	S	0.46	0.01
5OQV	Aβ_{42}	L−S	0.34	0.00
2M4J	Aβ_{40}	U	0.00	0.03
2BEG	Aβ_{42}	U	0.01	0.03
2LMN	Aβ_{40}	U	0.00	0.05
any			1.24	0.12
β-strand	Aβ_{40}	U	9	2

^{a}The same reference peptide segment (17−40) was used to calculate RMSD values, whereas region 30−40 is analyzed for β-strand conformation. The following chains have been used from PDB models 1: 2MXU,[75] chain A; 2NAO,[76] chain B; 5KK3,[77] chain E; 5OQV,[65] chain B; 2M4J,[69] chain D; 2BEG,[78] chain C; and 2LMN,[79] chain D.

with low free energy are displayed for Cu−Aβ_{40} (right panel), whereas 3 are displayed with no bound Cu (left panel). All of the peaks in the landscape with Cu are narrower than that in the absence of Cu, consistently with the distributions of geometrical parameters reported in Figure 2. The most representative structures of the maximally populated peaks (peak 1) are characterized by a larger content of secondary motifs when Cu is bound to the peptide (Figure 5C compared to Figure 5A). The comparison between secondary peaks, like peak 3 in Figure 4, displays that with no Cu, the U shape of the C-terminus appears (top left in Figure 5B), with the Asp 1 side chain taken apart within a more structured N-terminus. With Cu binding (Figure 5D), the structure is more sparse along with the chain and the U shape in the C-terminus is hindered. When Cu is bound to the peptide, His 14 is often involved in interactions with the Phe−Phe hydrophobic segment, whereas in the absence of Cu, His 14 is more involved in clusters involving His 13 and Val 40, as it is also shown by the hydrogen bond population (see Table 3). In the latter conditions, the hydrophobic Phe−Phe segment is more suitable for intermolecular interactions favoring interpeptide clusters.

Representative structures of peaks 1−2 in Figure 4 are all characterized by low values of gyration radius, $R_g \simeq 1$ nm. These configurations represent contributions to compact conformations evident from ion mobility experiments (see above). On the other hand, configurations representative of
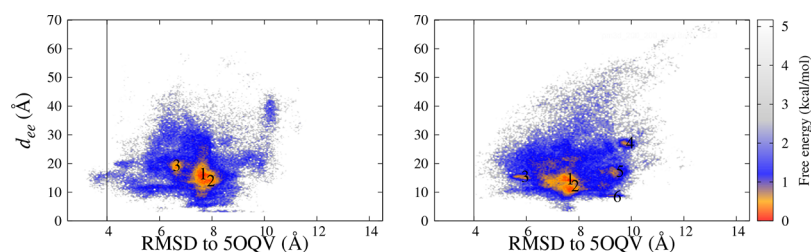
Figure 4. Free-energy landscape for $A\beta_{40}$ (left) and $Cu-A\beta_{40}$ (right) at $T = 311$ K, as a function of end-to-end distance (d_{ee}) and RMSD with respect to PDB monomer C in model 1 of 5OQV (backbone of residues 17−40), after equilibration of 60 ns. The vertical line at RMSD = 4 Å indicates the limit used to calculate the percentage reported in Table 4.
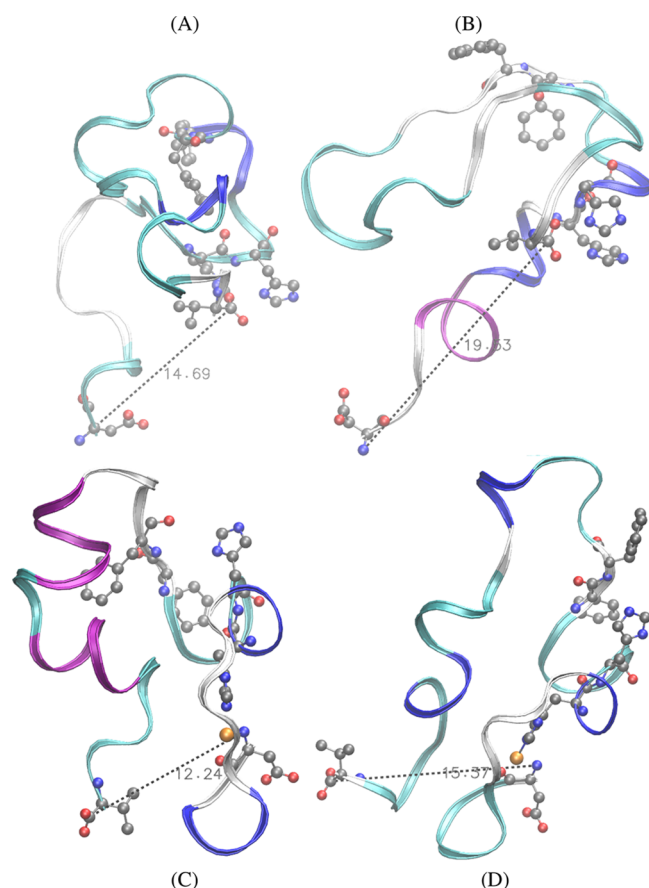

Figure 5. Structures representing the free-energy minima corresponding to peaks 1 (A) and 3 (B) for $A\beta_{40}$ (Figure 4, left) and peaks 1 (C) and 3 (D) for $Cu-A\beta_{40}$ (Figure 4, right). Ribbons interpolate peptide backbone; colors are associated with secondary motifs identified by the STRIDE[80] algorithm (α-helix is in magenta and blue, β-sheet is in yellow, turn is in cyan, and coil is in white). Residues Asp 1, His 13−14, Phe 19−20, and Val 40 are displayed. Atomic radii and bonds are arbitrary. The Cu ion is represented as an orange sphere. The VMD program[81] is used for molecular drawing.

peak 3 display $R_g = 1.00$ and 1.06 nm without Cu and with Cu, respectively: thus, as for the configurations contributing to peak 3, gyration radius and end-to-end distance are slightly anticorrelated. Peaks 4−6 in the right panel of Figure 4, i.e., those peaks present only in the Cu-bound peptide, contain structures with $R_g > 1.1$ nm. Therefore, peaks 4−6 show that a partial structure is induced by Cu binding in the domain of more extended configurations, consistently with the shape of $P(R_g)$ displayed in Figure 2A. Peak 6 contributes to d_{ee} of 0.9 nm, i.e., the second peak in $P(d_{ee})$ (Figure 2B). It is interesting

to notice that the first peak in the distribution of d_{ee} (at 0.3 nm, Figure 2B) at $T = 311$ K changes significantly with Cu binding. This shows that the release of the positive charge (the proton) due to Cu binding is not completely replaced by the positive charge in the Cu moiety. The major effect is the replacement of Val 40 with Tyr 10 because of the introduction of Cu in the N-terminus. This different arrangement of Tyr 10 has potential strong impact for the oxidoreductive properties of $Cu-A\beta_{40}$, being Tyr 10 a potential vehicle of unpaired electrons from the Cu center.

■ DISCUSSION

The 40-residue peptide $A\beta_{40}$ differs, in terms of biophysical properties, from the 42-residue long fragment $A\beta_{42}$. The latter is more toxic, less soluble in water, and forms fibrils at a higher rate.[9] On the other hand, in terms of the effects of Cu binding, the two peptides are more similar.[19] In both peptides, the 1:1 $Cu/A\beta$ ratio causes the formation of amorphous aggregates in place of β-rich aggregates, the latter configuration present at large extent in all of the fibril states structurally investigated so far for both $A\beta_{40}$ and $A\beta_{42}$.

The REMD simulation of the monomeric forms of $A\beta_{40}$ and $Cu-A\beta_{40}$, the latter with Cu bound to the peptide as in the prevailing physiological form consistent with in vitro experiments, allows a comparison with the 1 μs MD simulations previously performed for $A\beta_{42}$ and $Cu-A\beta_{42}$, with the same type of Cu binding to the peptide, at the slightly lower temperature T of 300 K. These data are reported in Figure 1 and Table 1 of ref 22. A brief comparison is discussed below.

As for the increase of SASA, the effect of Cu binding is in the same direction in the two peptides, with a more significant effect in $A\beta_{42}$: ΔSASA is 4.4 nm^2 when Cu is bound to $A\beta_{42}$, compared to 1.6 nm^2 in $A\beta_{40}$ at $T = 300$ K and 1.1 nm^2 at $T = 311$ K. The detailed analysis of SBs in the canonical MD simulation at $T = 300$ K of $A\beta_{42}$ monomers revealed that the monomer with no Cu has more freedom to form intradomain SBs, including the Asp 23−Lys 28 SB that stabilizes the U-shape in the C-terminus of the peptide. For instance, this important intradomain SB is released when Cu is bound to the N-terminus of $A\beta_{42}$ because of the larger involvement of charged side chains in interactions between two domains, one in the N-terminus and the other in the C-terminus. As a consequence, the total number of SBs for monomers increased when Cu was introduced in the $A\beta_{42}$ peptide. This picture does not hold for the REMD simulation of $A\beta_{40}$ presented here: the lower number of SBs observed when Cu is bound to the N-terminus does not imply a stronger cross-talk with the C-terminus, rather it lets the charged side chains to interact with the water solvent.

As for the number of intramolecular hydrogen bonds and β-sheet content, the change induced by Cu binding in Aβ_{42} is in the same direction of that found in REMD of Aβ_{40}: the number of hydrogen bonds increases, thus hindering the formation of intermolecular hydrogen bonds for Cu−Aβ_{42} dimers; the β-sheet content decreases, thus further disfavoring registers of intermolecular hydrogen bonds.

As for a monomer shape, the structures reported in the PDB for Aβ peptides differ significantly. Thus, only an average comparison is meaningful (last lines in Table 4). The most recent structure added to the PDB database, structure 5OQV, is for Aβ_{42}. This structure reports for the first time an organized location of the N-terminus, forming the L−S shape, with L the N-terminus and S the C-terminus. This information allows a more accurate estimate of the monomer shape and, in particular, the entire monomer adopts a flat shape. Comparing with the other structures reported in the PDB (see Table 4), the increasing flatness of the monomer, starting from the C-terminus (all PDB structures) and continuing toward the N-terminus (the most recent 5OQV structure), appears as a common feature of Aβ_{40} and Aβ_{42}. The extent of cross-talking between termini, both within the same monomer and within different monomers, depends on the sequence and composition of the two termini, but on average, the propensity for flat shapes is affected in the same direction by Cu binding to the N-terminus.

A wide REMD statistics for Aβ_{42} is required to make a full comparison between the two peptides because in canonical MD, extended peptide configurations are rarely sampled even in the microsecond timescale. Nevertheless, the comparison summarized above shows that in both cases (Aβ_{40} and Aβ_{42}), the Cu binding hinders configurations prone to extended aggregates with monomers' shape suited to fibril structure. However, this hindering effect is differently operated in the two cases, indicating that the type of polymorphism induced by Cu binding is modulated by the sequence in the C-terminus of the peptide.

CONCLUSIONS

We analyzed, by molecular modeling, an extensive statistical sampling of Aβ_{40} as a monomer, with the aim at understanding if the binding of the monomer to a single copper ion, as in the prevailing coordination mode observed experimentally, has a significant effect in preorganizing the peptide to either hinder or enhance specific intermolecular interactions, at the temperature of the synaptic region (T = 311 K).

We found that the effect of Cu binding is in favoring different molecular shapes, characterized by a larger size and SASA compared to the peptide in the absence of Cu, even though the small population of compact conformers is increased, consistently with ion mobility MS data. This change in average shape is correlated with a larger number of intramolecular hydrogen bonds involving the backbone amide N−H bonds and with a smaller number of interactions between charged groups (SBs). The Cu binding introduces significant structural diversity in the peptide, producing a polymorphic state characterized by more segregated conformations compared to the Cu-free peptide. Because of the larger structural plasticity, the peptide with no bound Cu samples with significant probability configurations similar to most of the experimental structures of the amyloid fibril. The structure introduced in the peptide by Cu binding, on the other hand, hinders, on average, such configurations. This

behavior of Cu−Aβ increases the latency of soluble forms, not strongly embedded in protofibrils similar to that in the absence of Cu.

This analysis confirms, by more robust computational methods, the conclusions derived with a lower sampling (ref 22): compared to the monomer with no Cu, the Cu binding enhances the probability of different segregated shapes (i.e., induces polymorphism) and of conformations with a larger extent of interactions with the water solvent. In these conditions, a better access to the molecule is possible for ions and reactant in the water solution. The different hydrated shapes adopted by Cu−Aβ_{40} better fit into amorphous and reactive phases compared to elongated protofibrils because of the propensity for a well-defined peptide shape and lower hydration in the latter type of assembly. In conclusion, the structural models here provided support for the higher toxicity of Aβ peptides when in the presence of copper in the 1:1 ratio.

AUTHOR INFORMATION

Corresponding Authors
*E-mail: masli@ifpan.edu.pl (M.S.L.).
*E-mail: giovanni.lapenna@cnr.it (G.L.P.).

ORCID
Mai Suan Li: 0000-0001-7021-7916
Giovanni La Penna: 0000-0002-8619-4867

Notes
The authors declare no competing financial interest.

REFERENCES

(1) Wilson, R. S.; Segawa, E.; Boyle, P. A.; Anagnos, S. E.; Hizel, L. P.; Bennett, D. A. The natural history of cognitive decline in Alzheimer's disease. *Psychol. Aging* **2012**, *27*, 1008−1017.

(2) Hardy, J.; Selkoe, D. J. The amyloid hypothesis of Alzheimer's disease: progress and problems on the road to therapeutics. *Science* **2002**, *297*, 353−356.

(3) Alonso, A. d. C.; Zaidi, T.; Novak, M.; Grundke-Iqbal, I.; Iqbal, K. Hyperphosphorylation induces self-assembly of into tangles of paired helical filaments/straight filaments. *Proc. Natl. Acad. Sci. U.S.A.* **2001**, *98*, 6923−6928.

(4) Fitzpatrick, A. W. P.; Debelouchina, G. T.; Bayro, M. J.; Clare, D. K.; Caporini, M. A.; Bajaj, V. S.; Jaroniec, C. P.; Wang, L.; Ladizhansky, V.; Müller, S. A.; et al. Atomic structure and hierarchical assembly of a cross-β amyloid fibril. *Proc. Natl. Acad. Sci. U.S.A.* **2013**, *110*, 5468−5473.

(5) Straub, J. E.; Thirumalai, D. Toward a molecular theory of early and late events in monomer to amyloid fibril formation. *Annu. Rev. Phys. Chem.* **2011**, *62*, 437−463.

(6) Chiang, K.; Koo, E. H. Emerging therapeutics for Alzheimer's disease. *Annu. Rev. Pharmacol. Toxicol.* **2014**, *54*, 381−405.

(7) Lesné, S.; Koh, M. T.; Kotilinek, L.; Kayed, R.; Glabe, C. G.; Yang, A.; Gallagher, M.; Ashe, K. H. A specific amyloid-β protein assembly in the brain impairs memory. *Nature* **2006**, *440*, 352−357.

(8) Selkoe, D. J. Soluble oligomers of the amyloid β-protein impair synaptic plasticity and behavior. *Behav. Brain Res.* **2008**, *192*, 106−113.

(9) Bernstein, S. L.; Dupuis, N. F.; Lazo, N. D.; Wyttenbach, T.; Condron, M. M.; Bitan, G.; Teplow, D. B.; Shea, J.-E.; Ruotolo, B. T.; Robinson, C. V.; et al. Amyloid-β protein oligomerization and the importance of tetramers and dodecamers in the aetiology of Alzheimer's disease. *Nat. Chem.* **2009**, *1*, 326−331.

(10) Nag, S.; Sarkar, B.; Bandyopadhyay, A.; Sahoo, B.; Sreenivasan, V. K. A.; Kombrabail, M.; Muralidharan, C.; Maiti, S. Nature of the Amyloid-β Monomer and the Monomer-Oligomer Equilibrium. *J. Biol. Chem.* **2011**, *286*, 13827−13833.

(11) Hayden, E. Y.; Teplow, D. B. Amyloid β-protein oligomers and Alzheimer's disease. *Alzheimer's Res. Ther.* **2013**, *5*, 60.

(12) Wolff, M.; Unuchek, D.; Zhang, B.; Gordeliy, V.; Willbold, D.; Nagel-Steger, L. Amyloid β Oligomeric Species Present in the Lag Phase of Amyloid Formation. *PLoS One* **2015**, *10*, e0127865. , Abeta hexamers

(13) Faller, P.; Hureau, C.; La Penna, G. Metal Ions and Intrinsically Disordered Proteins and Peptides: From Cu/Zn Amyloid-β to General Principles. *Acc. Chem. Res.* **2014**, *47*, 2252−2259.

(14) Lovell, M. A.; Robertson, J. D.; Teesdale, W. J.; Campbell, J. L.; Markesbery, W. R. Copper, iron and zinc in Alzheimer's disease senile plaques. *J. Neurol. Sci.* **1998**, *158*, 47−52.

(15) Miller, L. M.; Wang, Q.; Telivala, T. P.; Smith, R. J.; Lanzirotti, A.; Miklossy, J. Synchrotron-based infrared and X-ray imaging shows focalized accumulation of Cu and Zn co-localized with β-amyloid deposits in Alzheimer's disease. *J. Struct. Biol.* **2006**, *155*, 30−37.

(16) Maynard, C. J.; Bush, A. I.; Masters, C. L.; Cappai, R.; Li, Q.-X. Metals and amyloid-β in Alzheimer's disease. *Int. J. Exp. Pathol.* **2005**, *86*, 147−159.

(17) Barnham, K. J.; Bush, A. I. Metals in Alzheimer's and Parkinson's diseases. *Curr. Opin. Chem. Biol.* **2008**, *12*, 222−228.

(18) Barnham, K. J.; Bush, A. I. Biological metals and metal-targeting compounds in major neurodegenerative diseases. *Chem. Soc. Rev.* **2014**, *43*, 6727−6749.

(19) Pedersen, J. T.; Østergaard, J.; Rozlosnik, N.; Gammelgaard, B.; Heegaard, N. H. H. Cu(II) Mediates Kinetically Distinct, Non-amyloidogenic Aggregation of Amyloid-β Peptides. *J. Biol. Chem.* **2011**, *286*, 26952−26963.

(20) Mirats, A.; Alí-Torres, J.; Rodríguez-Santiago, L.; Sodupe, M.; La Penna, G. Dioxygen activation in the Cu-amyloid β complex. *Phys. Chem. Chem. Phys.* **2015**, *17*, 27270−27274.

(21) Reybier, K.; Ayala, S.; Alies, B.; Rodrigues, J. V.; Bustos Rodriguez, S.; La Penna, G.; Collin, F.; Gomes, C. M.; Hureau, C.; Faller, P. Free Superoxide is an Intermediate in the Production of H2O2 by Copper(I)-Aβ Peptide and O2. *Angew. Chem., Int. Ed.* **2016**, *55*, 1085−1089.

(22) Huy, P. D. Q.; Vuong, Q. V.; La Penna, G.; Faller, P.; Li, M. S. Impact of Cu(II) Binding on Structures and Dynamics of Aβ42 Monomer and Dimer: Molecular Dynamics Study. *ACS Chem. Neurosci.* **2016**, *7*, 1348−1363.

(23) La Penna, G.; Li, M. S. Towards a high-throughput modelling of copper reactivity induced by structural disorder in amyloid peptides. *Chem.—Eur. J.* **2018**, *24*, 5259−5270.

(24) Miller, Y.; Ma, B.; Nussinov, R. Metal binding sites in amyloid oligomers: Complexes and mechanisms. *Coord. Chem. Rev.* **2012**, *256*, 2245−2252.

(25) Drew, S. C.; Masters, C. L.; Barnham, K. J. Alanine-2 carbonyl is an oxygen ligand in Cu2+ coordination of Alzheimer's disease amyloid-β peptide: Relevance to N-terminally truncated forms. *J. Am. Chem. Soc.* **2009**, *131*, 8760−8761.

(26) Dorlet, P.; Gambarelli, S.; Faller, P.; Hureau, C. Pulse EPR spectroscopy reveals the coordination sphere of copper(II) ions in the 1-16 amyloid-β peptide: A key role of the first two N-terminus residues. *Angew. Chem., Int. Ed.* **2009**, *48*, 9273−9276.

(27) Miura, T.; Suzuki, K.; Kohata, N.; Takeuchi, H. Metal binding modes of Alzheimer's amyloid β-peptide in insoluble aggregates and soluble complexes. *Biochemistry* **2000**, *39*, 7024−7031.

(28) Hou, L.; Zagorski, M. G. NMR reveals anomalous copper(II) binding to the amyloid Aβ peptide of Alzheimer's disease. *J. Am. Chem. Soc.* **2006**, *128*, 9260−9261.

(29) Parthasarathy, S.; Long, F.; Miller, Y.; Xiao, Y.; McElheny, D.; Thurber, K.; Ma, B.; Nussinov, R.; Ishii, Y. Molecular-level examination of Cu2+ binding structure for amyloid fibrils of 40-residue Alzheimer's β by solid-state NMR spectroscopy. *J. Am. Chem. Soc.* **2011**, *133*, 3390−3400.

(30) Minicozzi, V.; Stellato, F.; Comai, M.; Serra, M. D.; Potrich, C.; Meyer-Klaucke, W.; Morante, S. Identifying the Minimal Copper- and Zinc-binding Site Sequence in Amyloid-β Peptides. *J. Biol. Chem.* **2008**, *283*, 10784−10792.

(31) Gomez-Castro, C. Z.; Vela, A.; Quintanar, L.; Grande-Aztatzi, R.; Mineva, T.; Goursot, A. Insights into the Oxygen-Based Ligand of the Low pH Component of the Cu2+-Amyloid-β Complex. *J. Phys. Chem. B* **2014**, *118*, 10052−10064.

(32) Ryan, T. M.; Kirby, N.; Mertens, H. D. T.; Roberts, B.; Barnham, K. J.; Cappai, R.; Pham, C. L. L.; Masters, C. L.; Curtain, C. C. Small angle X-ray scattering analysis of Cu2+ -induced oligomers of the Alzheimer's amyloid β-peptide. *Metallomics* **2015**, *7*, 536−543.

(33) Sitkiewicz, E.; Kłoniecki, M.; Poznański, J.; Bal, W.; Dadlez, M. Factors Influencing Compact-Extended Structure Equilibrium in Oligomers of Aβ1-40 Peptide-An Ion Mobility Mass Spectrometry Study. *J. Mol. Biol.* **2014**, *426*, 2871−2885.

(34) Bitan, G.; Vollers, S. S.; Teplow, D. B. Elucidation of Primary Structure Elements Controlling Early Amyloid β-Protein Oligomerization. *J. Biol. Chem.* **2003**, *278*, 34882−34889.

(35) Innocenti, M.; Salvietti, E.; Guidotti, M.; Casini, A.; Bellandi, S.; Foresti, M. L.; Gabbiani, C.; Pozzi, A.; Zatta, P.; Messori, L. Trace Copper(II) or Zinc(II) Ions Drastically Modify the Aggregation Behavior of Amyloid-β1-42: An AFM Study. *J. Alzheim. Dis.* **2010**, *19*, 1323−1329.

(36) Hane, F.; Tran, G.; Attwood, S. J.; Leonenko, Z. Cu2+ Affects Amyloid-β (1-42) Aggregation by Increasing Peptide-Peptide Binding Forces. *PLoS One* **2013**, *8*, e59005.

(37) Ono, K.; Condron, M. M.; Teplow, D. B. Structure-neurotoxicity relationships of amyloid -protein oligomers. *Proc. Natl. Acad. Sci. U.S.A.* **2009**, *106*, 14745−14750.

(38) Huang, T. H. J.; Yang, D.-S.; Plaskos, N. P.; Go, S.; Yip, C. M.; Fraser, P. E.; Chakrabartty, A. Structural studies of soluble oligomers of the alzheimer β-amyloid peptide. *J. Mol. Biol.* **2000**, *297*, 73−87.

(39) Drew, S. C.; Barnham, K. J. The heterogeneous nature of Cu2+ interactions with Alzheimer's amyloid-β peptide. *Acc. Chem. Res.* **2011**, *44*, 1146−1155.

(40) Miller, Y.; Ma, B.; Nussinov, R. Zinc ions promote Alzheimer A aggregation via population shift of polymorphic states. *Proc. Natl. Acad. Sci. U.S.A.* **2010**, *107*, 9490−9495.

(41) Miller, Y.; Ma, B.; Nussinov, R. Polymorphism in Alzheimer Aβ Amyloid Organization Reflects Conformational Selection in a Rugged Energy Landscape. *Chem. Rev.* **2010**, *110*, 4820−4838.

(42) Xu, L.; Wang, X.; Shan, S.; Wang, X. Characterization of the polymorphic states of copper(II)-bound Aβ(1-16) peptides by computational simulations. *J. Comput. Chem.* **2013**, *34*, 2524−2536.

(43) Sugita, Y.; Okamoto, Y. Replica-exchange molecular dynamics method for protein folding. *Chem. Phys. Lett.* **1999**, *314*, 141−151.

(44) Zhou, R. Replica exchange molecular dynamics method for protein folding simulation. In *Protein Folding Protocols*; Bai, Y., Nussinov, R., Eds.; Methods in Molecular Biology; Humana Press Inc., 2007; Vol. *350*, Chapter 12, pp 205−223.

(45) Jiang, P.; Yaşar, F.; Hansmann, U. H. E. Sampling of protein folding transitions: Multicanonical versus replica exchange molecular dynamics. *J. Chem. Theor. Comput.* **2013**, *9*, 3816−3825.

(46) Xi, W.; Hansmann, U. H. E. Conversion between parallel and antiparallel β-sheets in wild-type and Iowa mutant Aβ40 fibrils. *J. Chem. Phys.* **2018**, *148*, 045103.

(47) Case, D.; Babin, V.; Berryman, J.; Betz, R.; Cai, Q.; Cerutti, D.; Cheatham, T.; Darden, T.; Duke, R.; Gohlke, H.; et al. *Amber 14*; University of California at San Francisco: San Francisco, USA, 2014.

(48) Hornak, V.; Abel, R.; Okur, A.; Strockbine, B.; Roitberg, A.; Simmerling, C. Comparison of multiple Amber force fields and development of improved protein backbone parameters. *Proteins: Struct., Funct., Bioinf.* **2006**, *65*, 712−725.

(49) Jorgensen, W. L.; Chandrasekhar, J.; Madura, J. D.; Impey, R. W.; Klein, M. L. Comparison of simple potential functions for simulating liquid water. *J. Chem. Phys.* **1983**, *79*, 926−935.

(50) Huang, J.; Rauscher, S.; Nawrocki, G.; Ran, T.; Feig, M.; de Groot, B. L.; Grubmüller, H.; MacKerell, A. D., Jr. CHARMM36m: An improved force field for folded and intrinsically disordered proteins. *Nat. Methods* **2017**, *14*, 71−73. DOI: 10.1038/nmeth.4067. http://mackerell.umaryland.edu/charmm_ff.shtml.

(51) Kirkitadze, M. D.; Condron, M. M.; Teplow, D. B. Identification and characterization of key kinetic intermediates in amyloid *β*-protein fibrillogenesis11Edited by F. Cohen. *J. Mol. Biol.* **2001**, *312*, 1103−1119.

(52) Bayly, C. I.; Cieplak, P.; Cornell, W.; Kollman, P. A. A Well-behaved Electrostatic Potential Based Method Using Charge Restraints for Deriving Atomic Charges: the RESP Model. *J. Phys. Chem.* **1993**, *97*, 10269−10280.

(53) Cornell, W. D.; Cieplak, P.; Bayly, C. I.; Kollman, P. A. Application of RESP charges to calculate conformational energies, hydrogen bond energies, and free energies of solvation. *J. Am. Chem. Soc.* **1993**, *115*, 9620−9631.

(54) Comba, P.; Remenyi, R. A new molecular mechanics force field for the oxidized form of blue copper proteins. *J. Comput. Chem.* **2002**, *23*, 697−705.

(55) Wu, X.; Brooks, B. R. Self-guided langevin dynamics simulation method. *Chem. Phys. Lett.* **2003**, *381*, 512−518.

(56) Ryckaert, J.-P.; Ciccotti, G.; Berendsen, H. J. C. Numerical integration of the cartesian equations of motion of a system with constraints: molecular dynamics of n-alkanes. *J. Comput. Phys.* **1977**, *23*, 327−341.

(57) Darden, T.; York, D.; Pedersen, L. Particle mesh Ewald: An N·log(N) method for Ewald sums in large systems. *J. Chem. Phys.* **1993**, *98*, 10089−10092.

(58) Kumar, S.; Rosenberg, J. M.; Bouzida, D.; Swendsen, R. H.; Kollman, P. A. Multidimensional free-energy calculations using the weighted histogram analysis method. *J. Comput. Chem.* **1995**, *16*, 1339−1350.

(59) Kabsch, W. A solution for the best rotation to relate two sets of vectors. *Acta Crystallogr., Sect. A: Found. Adv.* **1976**, *32*, 922−923.

(60) Kabsch, W.; Sander, C. Dictionary of protein secondary structure: Pattern recognition of hydrogen-bonded and geometrical features. *Biopolymers* **1983**, *22*, 2577−2637.

(61) Weiser, J.; Shenkin, P. S.; Still, W. C. Approximate atomic surfaces from linear combinations of pairwise overlaps (LCPO). *J. Comput. Chem.* **1999**, *20*, 217−230.

(62) Theodorou, D. N.; Suter, U. W. Shape of unperturbed linear polymers: Polypropylene. *Macromolecules* **1985**, *18*, 1206−1214.

(63) Barducci, A.; Chelli, R.; Procacci, P.; Schettino, V.; Gervasio, F. L.; Parrinello, M. Metadynamics Simulation of Prion Protein: *β*-Structure Stability and the Early Stages of Misfolding. *J. Am. Chem. Soc.* **2006**, *128*, 2705−2710.

(64) Kłoniecki, M.; Jabłonowska, A.; Poznański, J.; Langridge, J.; Hughes, C.; Campuzano, I.; Giles, K.; Dadlez, M. Ion mobility separation coupled with MS detects two structural states of Alzheimer's disease A*β*1-40 peptide oligomers. *J. Mol. Biol.* **2011**, *407*, 110−124.

(65) Gremer, L.; Schölzel, D.; Schenk, C.; Reinartz, E.; Labahn, J.; Ravelli, R. B. G.; Tusche, M.; Lopez-Iglesias, C.; Hoyer, W.; Heise, H.; et al. Fibril structure of amyloid-*β*(1-42) by cryoelectron microscopy. *Science* **2017**, *358*, 116−119.

(66) Mesleh, M. F.; Hunter, J. M.; Shvartsburg, A. A.; Schatz, G. C.; Jarrold, M. F. Structural information from ion mobility measurements: Effects of the long-range potential. *J. Phys. Chem.* **1996**, *100*, 16082−16086. DOI: 10.1021/jp961623v. https://www.indiana.edu/nano/software/.

(67) Mesleh, M. F.; Hunter, J. M.; Shvartsburg, A. A.; Schatz, G. C.; Jarrold, M. F. Structural Information from Ion Mobility Measurements: Effects of the Long-Range Potential. *J. Phys. Chem. A* **1997**, *101*, 968.

(68) Shvartsburg, A. A.; Jarrold, M. F. An exact hard-spheres scattering model for the mobilities of polyatomic ions. *Chem. Phys. Lett.* **1996**, *261*, 86−91.

(69) Lu, J.-X.; Qiang, W.; Yau, W.-M.; Schwieters, C. D.; Meredith, S. C.; Tycko, R. Molecular structure of *β*-amyloid fibrils in Alzheimer's disease brain tissue. *Cell* **2013**, *154*, 1257−1268.

(70) Török, M.; Milton, S.; Kayed, R.; Wu, P.; McIntire, T.; Glabe, C. G.; Langen, R. Structural and dynamic features of Alzheimer's A*β* peptide in amyloid fibrils studied by site-directed spin labeling. *J. Biol. Chem.* **2002**, *277*, 40810−40815.

(71) Williams, A. D.; Portelius, E.; Kheterpal, I.; Guo, J.-t.; Cook, K. D.; Xu, Y.; Wetzel, R. Mapping A*β* Amyloid Fibril Secondary Structure Using Scanning Proline Mutagenesis. *J. Mol. Biol.* **2004**, *335*, 833−842.

(72) Tycko, R. Molecular structure of amyloid fibrils: Insights from solid-state NMR. *Q. Rev. Biophys.* **2006**, *39*, 1−55.

(73) Li, M. S.; Co, N. T.; Reddy, G.; Hu, C.-K.; Straub, J. E.; Thirumalai, D. Factors governing fibrillogenesis of polypeptide chains revealed by lattice models. *Phys. Rev. Lett.* **2010**, *105*, 218101.

(74) Qiang, W.; Yau, W.-M.; Luo, Y.; Mattson, M. P.; Tycko, R. Antiparallel -sheet architecture in Iowa-mutant -amyloid fibrils. *Proc. Natl. Acad. Sci. U.S.A.* **2012**, *109*, 4443−4448.

(75) Xiao, Y.; Ma, B.; McElheny, D.; Parthasarathy, S.; Long, F.; Hoshi, M.; Nussinov, R.; Ishii, Y. A*β*(1-42) fibril structure illuminates self-recognition and replication of amyloid in Alzheimer's disease. *Nat. Struct. Mol. Biol.* **2015**, *22*, 499−505.

(76) Wälti, M. A.; Ravotti, F.; Arai, H.; Glabe, C. G.; Wall, J. S.; Böckmann, A.; Güntert, P.; Meier, B. H.; Riek, R. Atomic-resolution structure of a disease-relevant A*β*(1-42) amyloid fibril. *Proc. Natl. Acad. Sci. U.S.A.* **2016**, *113*, E4976−E4984.

(77) Colvin, M. T.; Silvers, R.; Ni, Q. Z.; Can, T. V.; Sergeyev, I.; Rosay, M.; Donovan, K. J.; Michael, B.; Wall, J.; Linse, S.; et al. Atomic Resolution Structure of Monomorphic A*β*42 Amyloid Fibrils. *J. Am. Chem. Soc.* **2016**, *138*, 9663−9674.

(78) Luhrs, T.; Ritter, C.; Adrian, M.; Riek-Loher, D.; Bohrmann, B.; Dobeli, H.; Schubert, D.; Riek, R. 3D structure of Alzheimer's amyloid-*β*(1-42) fibrils. *Proc. Natl. Acad. Sci. U.S.A.* **2005**, *102*, 17342−17347.

(79) Paravastu, A. K.; Leapman, R. D.; Yau, W.-M.; Tycko, R. Molecular structural basis for polymorphism in Alzheimer's *β*-amyloid fibrils. *Proc. Natl. Acad. Sci. U.S.A.* **2008**, *105*, 18349−18354.

(80) Frishman, D.; Argos, P. Knowledge-based protein secondary structure assignment. *Proteins: Struct., Funct., Genet.* **1995**, *23*, 566−579.

(81) Humphrey, W.; Dalke, A.; Schulten, K. VMD: Visual molecular dynamics. *J. Mol. Graphics* **1996**, *14*, 33−38. DOI: 10.1016/0263-7855(96)00018-5. http://www.ks.uiuc.edu/Research/vmd.